IEEE Access
Multidisciplinary ⋮ Rapid Review ⋮ Open Access Journal

Received 16 August 2024, accepted 15 September 2024, date of publication 23 September 2024, date of current version 3 October 2024.

Digital Object Identifier 10.1109/ACCESS.2024.3466394

RESEARCH ARTICLE

Gaussian Process Regression-Based Control of Solids Circulation Rate in Dual Fluidized Bed Gasification

LUKAS STANGER[1], ALEXANDER BARTIK[2], MATTHIAS BINDER[2,3], ALEXANDER SCHIRRER[1], STEFAN JAKUBEK[1], AND MARTIN KOZEK[1]

[1]Institute of Mechanics and Mechatronics, TU Wien, 1060 Vienna, Austria
[2]Institute of Chemical, Environmental, and Bioscience Engineering, TU Wien, 1060 Vienna, Austria
[3]BEST-Bioenergy and Sustainable Technologies GmbH, 8010 Graz, Austria

Corresponding author: Lukas Stanger (lukas.stanger@tuwien.ac.at)

This work was supported in part by the Project Comprehensive Automation, Digitalisation and Optimization of Renewable and Sustainable SNG-production (ADORe-SNG), which is funded by the Austrian Research Promotion Agency (FFG) under Grant 881135; and in part by Technische Universität Wien (TU Wien) Bibliothek, Austria for financial support through its Open Access Funding Program.

ABSTRACT In dual fluidized bed (DFB) gasification, the solids circulation rate is critical as it determines the amount of char and heat transported between the interconnected reactors. In DFB plants, multiple control inputs are typically available to control the solids circulation rate, resulting in an over-actuated system. We propose a modeling and control method based on Gaussian process regression, a technique that provides a measure of confidence in the model prediction. The availability of redundant control inputs is resolved by explicitly incorporating the prediction confidence information into the control algorithm to drive the process in regions of low model uncertainty. To address plant-model mismatches, a disturbance model is employed, and an extended Kalman filter is used to estimate both system and disturbance states, enabling offset-free tracking of constant references. Modeling and closed-loop simulation results for both a 100 kW and a 1 MW DFB gasification plant demonstrate the applicability of the method to different plants. Experimental results are presented for the 100 kW plant, demonstrating the successful control of the circulation rate by the proposed algorithm.

INDEX TERMS Control, dual fluidized bed gasification, extended Kalman filter, Gaussian process regression, solids circulation rate.

I. INTRODUCTION

As the global energy demand continues to rise and greenhouse gas emissions have to be reduced, sustainable energy solutions are needed [1]. Gasification of biomass or residues can be employed to produce sustainable energy carriers. Dual fluidized bed (DFB) steam gasification represents a promising pathway to produce a product gas that is primarily composed of hydrogen, carbon monoxide, carbon dioxide, and methane [2]. This product gas can further be upgraded for example to synthetic natural gas [3], [4], Fischer-Tropsch liquids [5], [6], or pure hydrogen [7], [8]. These conversions have substantial potential for both the energy sector and chemical manufacturing, providing a versatile platform for generating clean fuels from renewable resources.

A DFB gasification plant essentially consists of two interconnected reactors, a gasification reactor (GR) and a combustion reactor (CR). Both reactors are operated as fluidized bed reactors. Bed material continuously circulates between those two reactors and transports heat from the CR to the GR and ungasified feedstock from the GR to the CR. The solids circulation rate is thus crucial for the process since it influences reactor temperatures as well as product gas composition and tar content [9]. Therefore, its efficient control is desired. Typically, multiple air inlets to the CR are available to control the circulation rate, resulting in redundant

The associate editor coordinating the review of this manuscript and approving it for publication was Ángel F. García-Fernández.

actuators for control. The mass of circulating bed material is difficult to measure. However, the pressure drop in the upper CR is a reliable indicator of the solids circulation rate [10].

To implement model-based control, a mathematical process model is needed. Studies on modeling the solids circulation in DFB gasification plants mainly rely on computational fluid dynamics (CFD), such as [11], [12]. Process simulation based on CFD requires high computational effort and is thus less practical for real-time control applications. An alternative approach is to use data-driven modeling approaches such as artificial neural networks as presented in [13]. A major challenge, thereby, is the limited availability of training data.

The application of Gaussian processes (GP) to regression problems has been presented in [14]. GP regression includes a measure of the prediction uncertainty in the model prediction. An application in control has been proposed in [15] for nonlinear systems that are linear in their input. For general nonlinear systems, an internal model controller has been presented in [16] and a model predictive control approach in [17].

Linear methods for controlling the solids circulation rate in DFB gasification plants have been proposed in [18] and [19]. However, these approaches are plant-specific and lack general applicability. To the best of the authors' knowledge, no nonlinear methods have been published in this context. This work addresses this gap by presenting an approach based on GP regression, as it can be used to map nonlinearities. Additionally, the method incorporates an explicit measure of uncertainty in its predictions. The presented control approach considers this uncertainty measure as well as the availability of redundant control actuators to drive the system into a region of low model uncertainty. In contrast to linear methods for solids circulation control, the method proposed in this work offers more flexibility and improved transferability to other plants. The method is applied to two different plants to demonstrate the ease of implementation across plants without extensive modeling efforts.

II. PROCESS DESCRIPTION

This section gives a concise overview of the DFB process, highlighting key information essential for controlling the solids circulation rate. In addition, the two plants considered in this paper are described: a pilot plant with 100 kW thermal fuel input and a demonstration plant with 1 MW thermal fuel input. Fig. 1 illustrates the design of the DFB gasification plants. Comprehensive descriptions of the DFB process can be found in [2] and [20]. Detailed information on the 100 kW pilot plant are given in [21] and [22], while more details on the 1 MW demonstration plant can be found in [23] and [24].

A. DUAL FLUIDIZED BED STEAM GASIFICATION

DFB steam gasification converts a feedstock, which can be biomass or biogenic residues, into a product gas by separating the gasification process taking place in the GR from the combustion process in the CR. These two interconnected reactors are both operated as fluidized bed reactors. The GR is operated as a bubbling fluidized bed reactor using steam as the gasification agent. The CR is operated as a fast fluidized bed reactor using air for fluidization. The bed material is constantly circulated between these two reactors. The feedstock is fed into the GR, where drying, devolatilization, and gasification take place. A portion of the feedstock remains ungasified and is transported as char by the bed material to the CR via a loop seal or chute at the bottom of the system. In the CR, the char is combusted, which heats the bed material. The hot bed material is returned to the GR through a loop seal at the top of the unit. The heat is required for the overall endothermic gasification reactions in the GR. The loop seals and chute, if present, are also fluidized by steam.

For better gas-solid interaction in the GR, a reactor design has been proposed in [25] that includes a countercurrent column above the freeboard in the GR. This design is intended to enhance the gas-solid contact and thus reduce the tar content in the product gas and increase the fuel flexibility of the process, allowing the gasification of low-cost feedstocks such as plastic waste. Both the 100 kW pilot plant and the 1 MW demonstration plant use this new design.

B. THE SOLIDS CIRCULATION RATE IN DFB GASIFICATION PLANTS

To adjust the solids circulation rate, the CR typically has multiple air inlets at different heights within the reactor. This design allows the solids circulation rate to be adjusted while maintaining the total amount of air required for complete combustion in the CR. Air introduced at lower levels of the reactor tends to lift the bed material upward, thereby increasing circulation. In contrast, air introduced at higher levels has less of an effect on circulation or may even reduce it.

Measurement of the solids circulation rate in circulating fluidized bed systems is challenging, and different approaches have been proposed. Several methods are reviewed in [26]. Some of them are based on interrupting the particle flow and measuring the accumulation of bed material as used in [27] and [28]. Other methods use optical measurements [29] or placing an obstacle in the flow and measuring the impact [30]. Other methods are based on measuring the pressure drop in the CR [10], [31], [32]. This method can be applied to industrial plants and is also applicable to hot plant operations. In this work, we directly interpret the pressure drop at the top of the CR as an indicator of the solids circulation rate and present a method to control it by adjusting the air staging in the CR.

C. DIFFERENCES IN THE DESIGN OF THE 100 KW PILOT PLANT AND THE 1 MW DEMONSTRATION PLANT

The design of the two DFB plants considered in this work is visualized in Fig. 1. The main differences are described below.

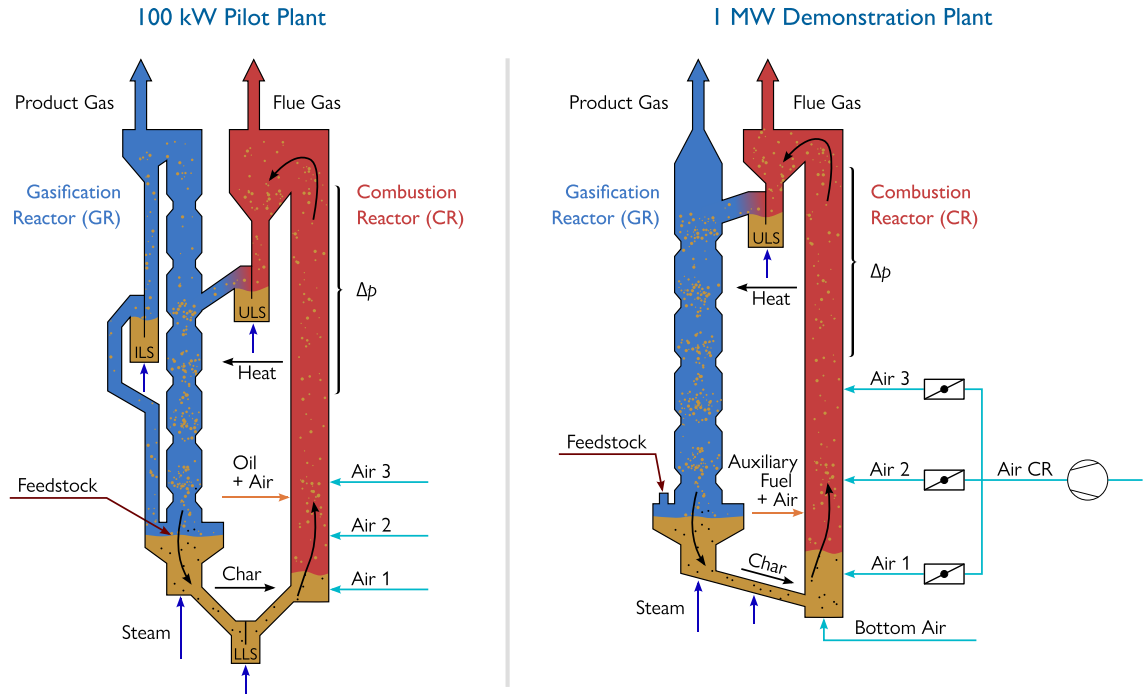

FIGURE 1. Design of the 100 kW pilot plant and the 1 MW demonstration plant, adopted from [13].

1) AIR SUPPLY TO THE CR

The most relevant process input variable for controlling the solids circulation rate is the air supply to the CR. In the 100 kW pilot plant, air can be supplied to the CR through three different air stages. The airflow is measured separately at each stage, and low-level controllers have been implemented to adjust the individual air streams as set by the plant operator or a high-level controller. For the 1 MW demonstration plant, in addition to the three air stages, there is a bottom air stage. The airflow through the bottom air stage to the CR is measured separately. For the other three air stages, only the total airflow is measured. This total airflow can be adjusted by changing the power of the compressor. The air can be distributed to the three air stages by adjusting the positions of the butterfly valves on the three stages. The valve for air 1 remains open during operation, and air is distributed by adjusting the valves for air 2 and air 3.

For both plants, additional air is supplied to the CR along with the auxiliary fuel. For the 100 kW pilot plant, a constant flow of 4 Nm^3/h is fed to the CR, while for the 1 MW demonstration plant, 40 Nm^3/h is provided.

2) LOWER LOOP SEAL AND CHUTE

For the 1 MW demonstration plant, a chute is used instead of a loop seal to connect the GR and the CR at the bottom. This is to allow the use of heterogeneous feedstocks, some of which also contain larger particles that could clog a loop seal.

3) AUXILIARY FUEL

To provide sufficient heat for the gasification reactions and for temperature control, auxiliary fuel is fed to the CR. For the 100 kW plant, heating oil is used. Auxiliary fuel is particularly necessary to compensate for the relatively high heat losses that occur at the pilot plant scale. Industrial plants typically do not use heating oil as an auxiliary fuel, but product gas can be recirculated to the CR. In the 1 MW plant, both fuel supply options are implemented. In addition, emulsion fluid from the product gas cleaning can be fed to the CR.

4) INTERNAL LOOP SEAL

For the 100 kW pilot plant, a gravity separator is used, and the separated particles are returned to the gasifier reactor (GR) via an internal loop seal. In the 1 MW demonstration plant, the product gas passes through a radiation cooler after exiting the GR, where the separated particles are then fed back to the GR (not shown in Fig. 1).

D. EXPERIMENTAL SETUP

Both plants are equipped with various measurement and actuation devices. The measurement and actuation equipment for the process variables presented in this work are listed in Table 1.

The experiments at the 100 kW pilot plant were conducted using softwood pellets as feedstock. The bed material consisted of a mixture of 80 % olivine and 20 % limestone.

Experiments at the 1 MW demonstration plant were conducted using olivine as the bed material, with the occasional addition of limestone to enhance catalytic activity. The test runs utilized various feedstocks, including wood

TABLE 1. Instrumentation for both the 100 kW pilot plant and the 1 MW demonstration plant.

	Process variable	Measurement	Actuator
100 kW	Pressure	Kalinsky pressure transmitter type DS1	-
	Air flows	Krohne H250	Bürkert electromotive 2 way globe proportional valve 3280
	Fuel feed	Rot. speed of dosing screws*	Motor with ABB ACS355 drive
1 MW	Pressure	Endress+Hauser PMC21	-
	Total air flow	Endress+Hauser Prowirl F 200	Elmo Rietschle (Gardner Denver) type DLR 301
	Bottom air	Endress+Hauser Prowirl F 200	Bürkert globe control valve 8802 GD with positioner 8692
	Fuel feed	Rot. speed of dosing screws*	SEW Eurodrive type KF77 DRN100LS4/V/PK gearmotor
	Valve positions	AGS butterfly valve RDB-L, pneumatic actuator PAG-E92-S10, limit switch box ELR.ER, Siemens SIPART PS2 valve positioner	

* The dosing screws are calibrated before every test run.

chips, softwood pellets, bark, forest residues, and a mixture of plastic residues and wood chips.

III. MODELING

This section describes the modeling approach used to model the pressure difference Δp in the upper CR, which represents the solids circulation rate. Given the nonlinearities present in the static input-output relationship, combined with the fact that the system dynamics can be adequately represented by a linear time-invariant (LTI) model, we employ a Hammerstein model. Fig. 2 visualizes the structure of the Hammerstein model and the model inputs used for the two different plants considered in this work. Preliminary studies have identified these model inputs as the process variables that most significantly affect the solids circulation rate. The model consists of a nonlinear static part and a linear dynamic part. We use GP regression for the static part to describe the input-output relationship at steady state, using steady-state process data as training data. The linear dynamic model captures the system dynamics and includes a disturbance model to account for plant model mismatch and unmeasured disturbances.

Additionally, artificial neural networks (ANNs) are utilized as simulation models for conducting closed-loop tests of the control algorithms, as described in the last part of this section. The use of ANNs allows the validation of the controller's performance against a model that is unknown to the controller. Furthermore, ANNs are chosen for their ability to model nonlinearities in the process.

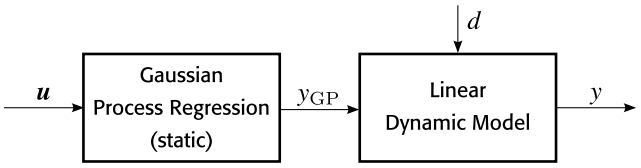

Inputs (u) 100 kW plant:
Feedstock (kg/h)
Air 1 (Nm^3/h)
Air 2 (Nm^3/h)
Air 3 (Nm^3/h)

Inputs (u) 1 MW plant:
Feedstock (kg/h)
Air CR (Nm^3/h)
Bottom air (Nm^3/h)
Valve air 2 (%)
Valve air 3 (%)

FIGURE 2. Hammerstein model structure and model inputs used for the two different DFB plants.

A. GAUSSIAN PROCESS REGRESSION

This section gives a brief introduction to GP regression. More detailed explanations can be found in [33] and [34].

Assuming a training dataset consisting of input measurements $\bar{\boldsymbol{U}} = [\bar{\boldsymbol{u}}_1, \ldots, \bar{\boldsymbol{u}}_N]$ and the corresponding output measurements $\bar{\boldsymbol{y}} = [\bar{y}_1, \ldots, \bar{y}_N]$. The goal is to predict a new output $\bar{y}_*$ given a new input vector $\bar{\boldsymbol{u}}_*$.

The outputs $\bar{\boldsymbol{y}} = [\bar{y}_1(\bar{\boldsymbol{u}}_1), \ldots, \bar{y}_N(\bar{\boldsymbol{u}}_N)]$ are assumed to be random variables with a joint normal distribution, thus

$$\bar{\boldsymbol{y}} \sim \mathcal{N}(\mu, \boldsymbol{C}), \tag{1}$$

where μ is the mean vector and $\boldsymbol{C}$ is the covariance matrix. In many applications, the mean vector is assumed to be the zero vector after the data has been appropriately scaled. The entries of the covariance matrix $\boldsymbol{C}$ are calculated using a covariance function $c(\cdot, \cdot)$, defined as

$$C_{ij} = c(\bar{\boldsymbol{u}}_i, \bar{\boldsymbol{u}}_j). \tag{2}$$

A popular choice for the covariance function is the squared exponential covariance function

$$c(\bar{\boldsymbol{u}}_i, \bar{\boldsymbol{u}}_j) = \sigma_f^2 \exp\left(-\frac{1}{2}\frac{\|\bar{\boldsymbol{u}}_i - \bar{\boldsymbol{u}}_j\|^2}{\sigma_l^2}\right) + \delta_{ij}\sigma_n^2, \tag{3}$$

where the hyperparameters $\theta = [\sigma_f, \sigma_l, \sigma_n]^T$ are governing the function's amplitude, length-scale, and noise level, respectively. The Kronecker delta δ_{ij} is defined as

$$\delta_{ij} = \begin{cases} 1 & \text{if } i = j, \\ 0 & \text{if } i \neq j. \end{cases} \tag{4}$$

This covariance function ensures that outputs $\bar{y}_i$ and $\bar{y}_j$ will have higher covariance if their corresponding inputs $\bar{\boldsymbol{u}}_i$ and $\bar{\boldsymbol{u}}_j$ are closer in the input space.

To predict a new output $\bar{y}_*$, a joint normal distribution is assumed for both the training points and the new data point, leading to

$$\begin{bmatrix} \bar{\boldsymbol{y}} \\ \bar{y}_* \end{bmatrix} \sim \mathcal{N}\left(\boldsymbol{0}, \begin{bmatrix} \boldsymbol{C} & \boldsymbol{c}_* \\ \boldsymbol{c}_*^T & c_{**} \end{bmatrix}\right), \tag{5}$$

where $\boldsymbol{c}_*$ is the covariance of the training outputs and the new output, given by

$$\boldsymbol{c}_* = c(\bar{\boldsymbol{U}}, \bar{\boldsymbol{u}}_*), \tag{6}$$

and c_{**} is the variance of the new input $\bar{\boldsymbol{u}}_*$, calculated as

$$c_{**} = c(\bar{\boldsymbol{u}}_*, \bar{\boldsymbol{u}}_*). \tag{7}$$

Given the observed training outputs $\bar{\boldsymbol{y}}$, the prediction for $\bar{y}_*$ is derived by computing the conditional normal distribution

$$\mu_* = \boldsymbol{c}_*^T \boldsymbol{C}^{-1} \bar{\boldsymbol{y}}, \tag{8a}$$
$$\sigma_*^2 = c_{**} - \boldsymbol{c}_*^T \boldsymbol{C}^{-1} \boldsymbol{c}_*, \tag{8b}$$

with the mean μ_* and the variance σ_* of the predicted output.

A common approach to training the hyperparameters θ, which is also used in this work, is to maximize the logarithmic marginal likelihood,

$$\log p(\bar{\boldsymbol{y}} \mid \boldsymbol{U}, \theta) = -\frac{1}{2}\bar{\boldsymbol{y}}^T \boldsymbol{C}^{-1} \bar{\boldsymbol{y}} - \frac{1}{2}\log \mid \boldsymbol{C} \mid - \frac{N}{2}\log 2\pi, \tag{9}$$

where $p(\bar{\boldsymbol{y}} \mid \boldsymbol{U}, \theta)$ is the probability that the training data was generated by the model given the input data and the hyperparameters.

Note that for each prediction, all the training data points are used, which can lead to a high computational effort for a large number of training data points. In [35], approximation methods are given to reduce this computational effort. In this work, the full data set is used to make predictions.

B. HAMMERSTEIN MODEL

GP regression is used to predict the output at steady state, hereinafter referred to as y_{GP}. In the real process, changes in input variables do not immediately affect the output. However, dynamic behavior can be observed. To incorporate these dynamics into the model, a linear dynamic model is used in series with the GP regression. In addition, a disturbance state is added to the model to account for plant model mismatch and unmeasured disturbances acting on the process. This disturbance state adds an integrator to the plant model, which later enables offset-free tracking of constant references. The resulting model is described by the differential equations

$$\begin{cases} \dot{x}(t) = \dfrac{1}{\tau}(-x(t) + y_{\mathrm{GP}}(\boldsymbol{u}(t)) + d(t)), \\ \dot{d}(t) = 0, \\ y(t) = x(t), \end{cases} \tag{10}$$

where $x(t)$ and $d(t)$ are the system state and the disturbance state, respectively.

Both the state estimator and the controller are implemented in discrete time. Therefore, the model is discretized assuming zero-order hold for the GP prediction y_{GP} and the disturbance state d, which leads to

$$\begin{cases} x_{k+1} = a x_k + b y_{\mathrm{GP}}(\boldsymbol{u}_k) + b d_k, \\ d_{k+1} = d_k, \\ y_k = x_k, \end{cases} \tag{11}$$

where

$$a = e^{-T_s/\tau}, \quad b = 1 - e^{-T_s/\tau}, \tag{12}$$

with the sampling time T_s. The GP prediction is a normally distributed random variable

$$y_{\mathrm{GP}} \sim \mathcal{N}(\mu_{\mathrm{GP}}, \sigma_{\mathrm{GP}}^2). \tag{13}$$

This can be decomposed to

$$y_{\mathrm{GP}} = \mu_{\mathrm{GP}} + \eta_{\mathrm{GP}}, \tag{14}$$

where

$$\eta_{\mathrm{GP}} \sim \mathcal{N}(0, \sigma_{\mathrm{GP}}^2). \tag{15}$$

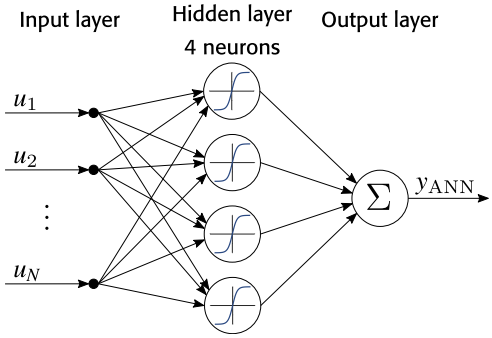

FIGURE 3. Structure of the artificial neural network (ANN) used as a simulation model in closed-loop simulations, where y_{ANN} represents the ANN's prediction.

C. ARTIFICIAL NEURAL NETWORKS AS SIMULATION MODELS

An ANN is trained for each plant using the same model inputs as those used for GP regression. Unlike GP regression, the ANNs are trained on time series data. Each ANN consists of a single hidden layer with four neurons and an output layer, as shown in Fig. 3. The neurons in the hidden layer use tangent sigmoid activation functions, while the output layer establishes a linear relationship between the outputs of the hidden layer neurons and the ANN's final output. Quasi-Newton backpropagation is used to train the networks using the MATLAB Deep Learning Toolbox [36].

IV. STATE ESTIMATION AND NONLINEAR CONTROL

A. EXTENDED KALMAN FILTER FOR STATE ESTIMATION

An extended Kalman filter (EKF) [37] is used to estimate both the system state x and the disturbance state d. It is assumed that zero mean white noise drives the disturbance state d and acts on the measured output y. For the system state x, it is assumed that the uncertainty originates solely from the

GP prediction, which is normally distributed with a known variance. This leads to the following model for the EKF:

$$\begin{cases} x_{k+1} = ax_k + b\mu_{\mathrm{GP}}(\boldsymbol{u}_k) + bd_k + b\eta_{\mathrm{GP}}(\boldsymbol{u}_k), \\ d_{k+1} = d_k + w_k, \\ y_k = x_k + v_k, \end{cases} \tag{16}$$

with

$$w_k \sim \mathcal{N}(0, \sigma_w^2), \quad v_k \sim \mathcal{N}(0, \sigma_v^2). \tag{17}$$

To estimate the states, first, a prediction step is carried out

$$\begin{aligned} \hat{x}_{k+1}^- &= a\hat{x}_k + b\mu_{\mathrm{GP}}(\boldsymbol{u}_k) + b\hat{d}_k, \\ \hat{d}_{k+1}^- &= \hat{d}_k, \\ \boldsymbol{P}_k^- &= \boldsymbol{F}\boldsymbol{P}_{k-1}\boldsymbol{F}^T + \boldsymbol{Q}_k, \end{aligned} \tag{18}$$

with the prediction of the state covariance matrix $\boldsymbol{P}_k^-$, the system matrix of the augmented system $\boldsymbol{F}$, and the covariance matrix of the process noise $\boldsymbol{Q}_k$, which are

$$\boldsymbol{F} = \begin{bmatrix} a & b \\ 1 & 0 \end{bmatrix}, \quad \boldsymbol{Q}_k = \begin{bmatrix} b^2\sigma_{\mathrm{GP}}^2 & 0 \\ 0 & \sigma_w^2 \end{bmatrix}. \tag{19}$$

The prediction step is followed by a correction step

$$\begin{aligned} \boldsymbol{k}_k &= \boldsymbol{P}_k^-\boldsymbol{h}^T(\boldsymbol{h}\boldsymbol{P}_k^-\boldsymbol{h}^T + r)^{-1} \\ \begin{bmatrix} \hat{x}_k \\ \hat{d}_k \end{bmatrix} &= \begin{bmatrix} \hat{x}_k^- \\ \hat{d}_k^- \end{bmatrix} + \boldsymbol{k}_k(y_k - \hat{x}_k^-) \\ \boldsymbol{P}_k &= (\boldsymbol{I} - \boldsymbol{k}_k\boldsymbol{h})\boldsymbol{P}_k^- \end{aligned} \tag{20}$$

with

$$r = \sigma_v^2, \quad \boldsymbol{h} = \begin{bmatrix} 1 & 0 \end{bmatrix}. \tag{21}$$

Note that no approximation by model linearization is necessary because the state equation is nonlinear only in the input, not in the state.

B. NONLINEAR CONTROLLER DESIGN

For the process under consideration, multiple control inputs are available to control a single output. In addition, the GP prediction includes information about the confidence of the prediction. These two aspects are considered in the control design: A steady-state input vector $\bar{\boldsymbol{u}}_k$ should be found so that the output meets the reference r_k at steady state. Since there is no unique solution to this problem, $\bar{\boldsymbol{u}}_k$ is computed by solving the optimization problem

$$\min_{\bar{\boldsymbol{u}}_k} J = \sigma_{\mathrm{GP}}^2(\bar{\boldsymbol{u}}_k) + \lambda\|\bar{\boldsymbol{u}}_k - \boldsymbol{u}_{k-1}\|, \tag{22a}$$

$$\text{subject to } \mu_{\mathrm{GP}}(\bar{\boldsymbol{u}}_k) = r_k - \hat{d}_k, \tag{22b}$$

$$\bar{\boldsymbol{u}}_k \in \mathbb{U}, \tag{22c}$$

at each time step k, assuming that there are regions in the input space with higher and regions with lower uncertainty in the GP prediction. The first term in the cost function (22a) represents the uncertainty of the GP prediction, which is, generally a non-convex function. To avoid large steps in the input space for small improvements in uncertainty, the second term is added to the cost function, with a weighting factor $\lambda \geq 0$. Constraint (22b) ensures that an input vector is found such that the GP prediction matches the reference corrected by the estimated disturbance state $\hat{d}_k$. This correction by the disturbance state enables offset-free tracking of a constant reference, despite plant model mismatch or unmeasured disturbances acting on the process, and incorporates the feedback in the closed-loop system. By restricting the input space with (22c), some inputs that should not be used by the controller to control the output, such as the feedstock feed rate, can be fixed. In addition, upper and lower bounds can be implemented for the control inputs.

Since the cost function is generally non-convex, we solve the optimization problem (22) multiple times with different initial conditions, where the different initial conditions are generated by Latin hypercube sampling [38]. The solution with the lowest value of the cost function is then selected from the feasible solutions. The cost function is minimized using `fmincon` from the MATLAB Optimization Toolbox [39].

The optimization problem (22) may be infeasible, e.g. if a reference is set to a value that can not be reached according to GP regression. In this case, an alternative optimization problem is solved as a fallback that minimizes the squared difference between the GP prediction and the reference, corrected by the estimated disturbance state, which is

$$\min_{\bar{\boldsymbol{u}}_k} J = (\mu_{\mathrm{GP}}(\bar{\boldsymbol{u}}_k) - r_k + \hat{d}_k)^2, \tag{23a}$$

$$\text{subject to } \sigma_\xi^2(\bar{\boldsymbol{u}}_k) \leq \sigma_{\mathrm{GP,max}} \tag{23b}$$

$$\bar{\boldsymbol{u}}_k \in \mathbb{U}. \tag{23c}$$

With (23b), an upper bound for the uncertainty of the model prediction $\sigma_{\mathrm{GP,max}}$ is established to prevent finding a solution in regions of the input space where limited model information is available. Constraint (23b) may still lead to infeasibility, which can be avoided by omitting it.

Up to this point, the control input has been selected to ensure that the output will match the reference at steady state. However, this approach can result in abrupt, step-like changes in the control input, e.g. if the reference is changed stepwise. Such rapid changes in the control input may not be desired by the operator and the excitation of higher modes, which are not represented in the model, can be avoided. This can be avoided by not applying $\bar{\boldsymbol{u}}_k$ directly, but by applying a first-order delayed input $\boldsymbol{u}_k$ to the process, calculated as

$$\boldsymbol{u}_k = (\boldsymbol{I} + \boldsymbol{R}_c)^{-1}(\boldsymbol{I}\bar{\boldsymbol{u}}_k + \boldsymbol{R}_c\boldsymbol{u}_{k-1}), \tag{24}$$

where $\boldsymbol{R}_c$ is a weighting matrix. For $\boldsymbol{R}_c = \boldsymbol{0}$, $\bar{\boldsymbol{u}}_k$ is applied to the process immediately, while higher values in $\boldsymbol{R}_c$ result in smoother control inputs.

V. RESULTS AND DISCUSSION

This section presents modeling and controller simulation results for both the 100 kW and the 1 MW plant. In addition, experimental closed-loop results are shown for the 100 kW plant. All of the algorithms are implemented in MATLAB.

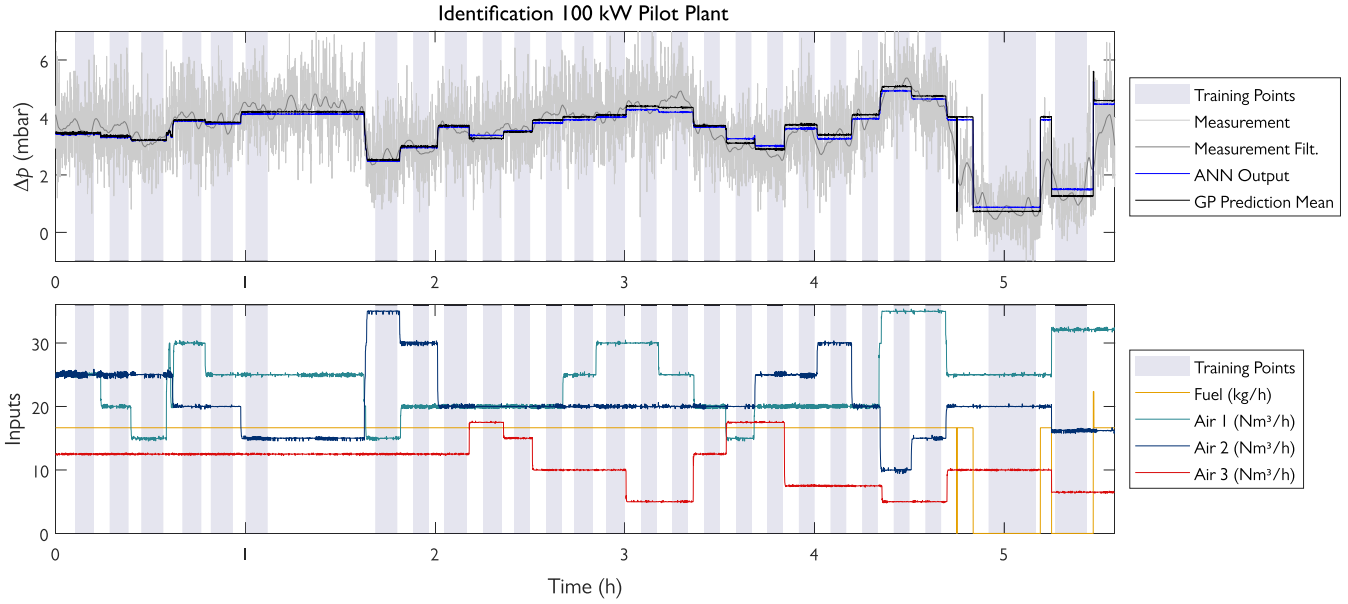

FIGURE 4. Identification data for the 100 kW demonstration plant with simulated output from GP regression and ANN.

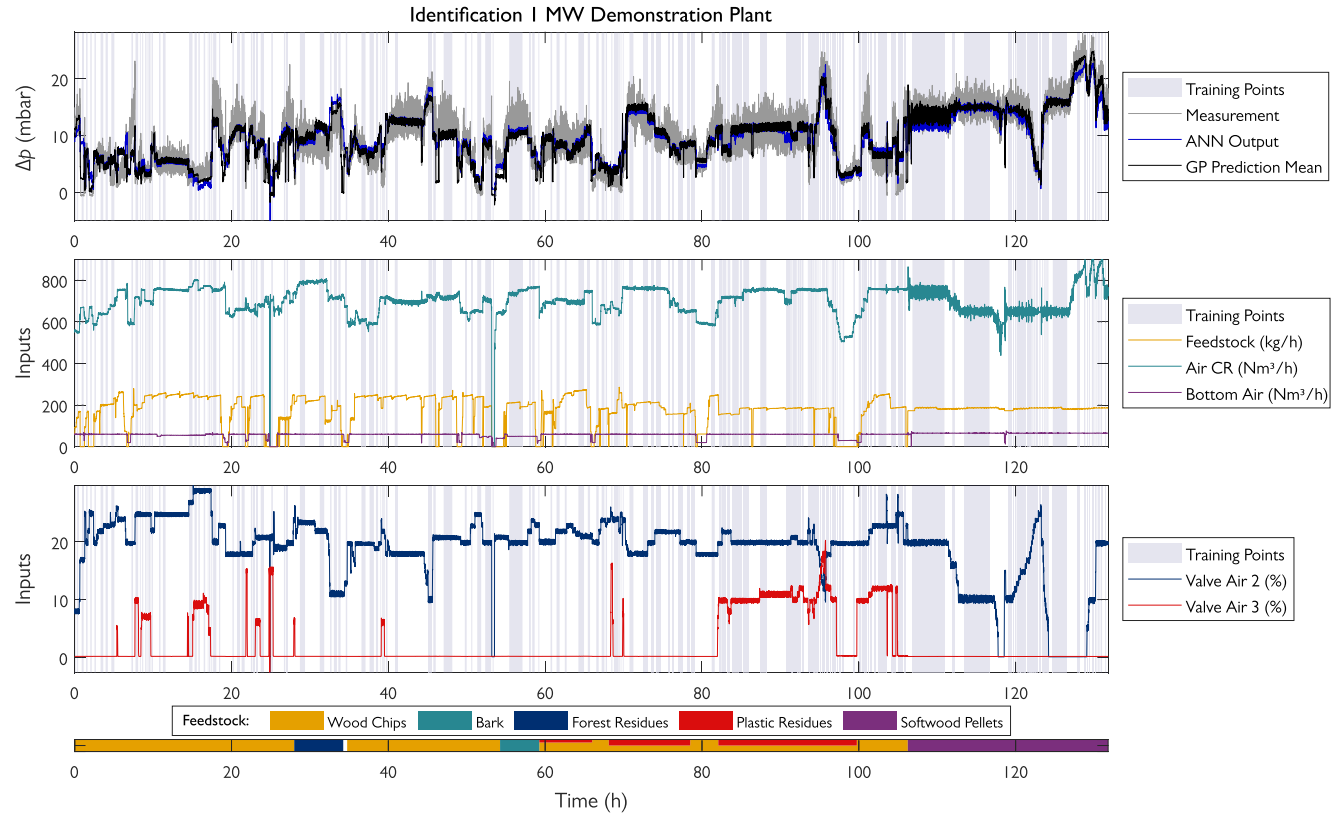

FIGURE 5. Identification data for the 1 MW demonstration plant with simulated output from GP regression and ANN.

The GP regression is implemented using the Statistics and Machine Learning Toolbox [40].

A. MODELING RESULTS

For both plants, data points from steady-state operation, represented as $\bar{\boldsymbol{U}}$ and $\bar{\boldsymbol{y}}$, are used as training points for the GP regression. These training points were manually selected by averaging the time series data over periods when the process was at steady state.

At the 100 kW pilot plant, an identification experiment was conducted to generate training data for the GP regression. Fig. 4 shows the time series data from this experiment.

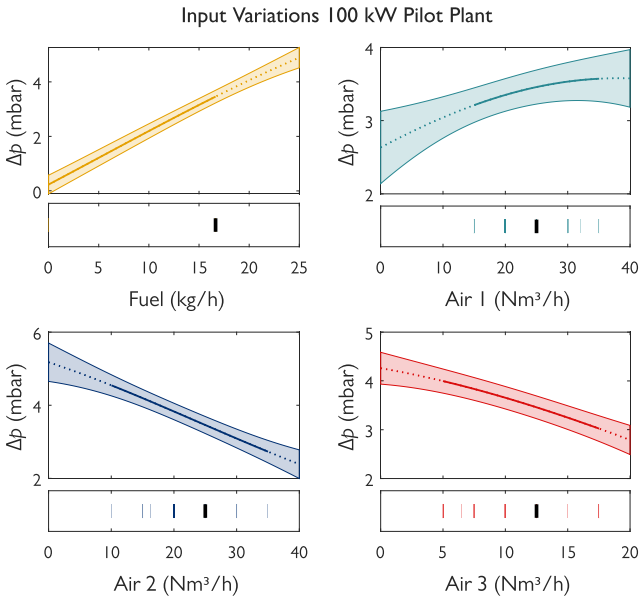

FIGURE 6. Variation of the inputs used by GP regression. The 4 inputs are varied individually from a starting point indicated by the black bars. The dotted lines indicate regions outside of where there are training data points.

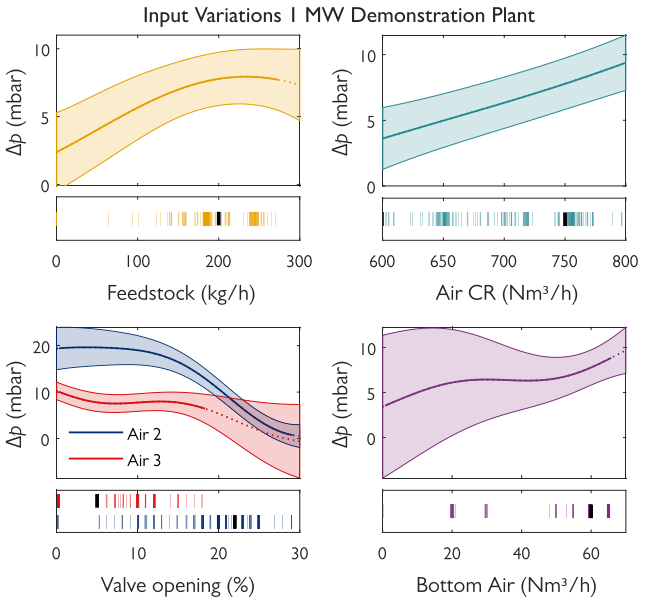

FIGURE 7. Variation of the inputs used by GP regression. The 5 inputs are varied individually from a starting point indicated by the black bars. The dotted lines indicate regions outside of where there are training data points.

TABLE 2. Computation times required for each time step in the closed-loop simulations.

	Calculation time	
	Mean	Max.
100 kW Pilot Plant	0.194 s	0.457 s
1 MW Demonstration Plant	0.277 s	0.528 s

The highlighted time periods indicate the steady-state points used as training points. The upper plot shows the pressure difference in the upper part of the CR, which represents the solids circulation rate. Both the raw measurement data and a filtered version are visualized. The filtering was performed using a 50-sample centered moving average. In addition, the predictions from both the GP regression and the ANN model are shown, generated by applying the respective models to the time series input data. The hyperparameters were identified as

$$\sigma_{l,100\text{kW}} = 11.58,\ \sigma_{f,100\text{kW}} = 4.962,\ \sigma_{n,100\text{kW}} = 0.2151.$$

Note that $\sigma^2_{n,100\text{kW}}$ is not the variance of the noise present in the time series data, since the data was averaged over measurement periods. However, noise can still be present due to disturbances that affect the output but are not accounted for in the model, such as variations in reactor temperature.

For the 1 MW demonstration plant, no specific identification experiments were conducted. Instead, measurement data from two different test runs, totaling approximately 136 hours of plant operation, was utilized. From these data, 201 points corresponding to steady-state operation were selected as training points for GP regression. Fig. 5 displays the measurement data, the selected training points,

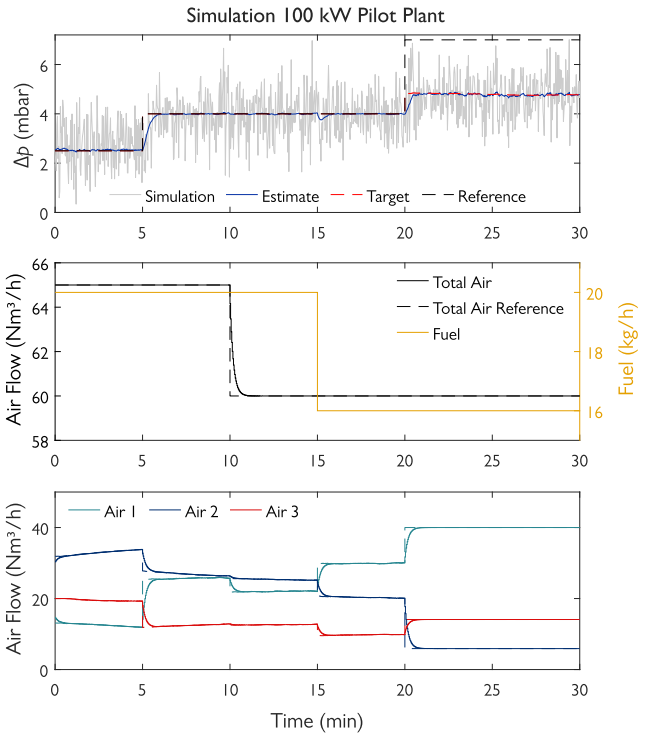

FIGURE 8. Closed-loop simulation results for the 100 kW pilot plant.

and predictions from both GP regression and the ANN. Additionally, the feedstock used is displayed at the bottom of the figure. When a mixture of plastic residues and wood chips was used, the height of the bar indicates the ratio, either 50:50 or 25:75. The hyperparameters were identified to be

$$\sigma_{l,1\text{MW}} = 1.998,\ \sigma_{f,1\text{MW}} = 8.844,\ \sigma_{n,1\text{MW}} = 1.828.$$

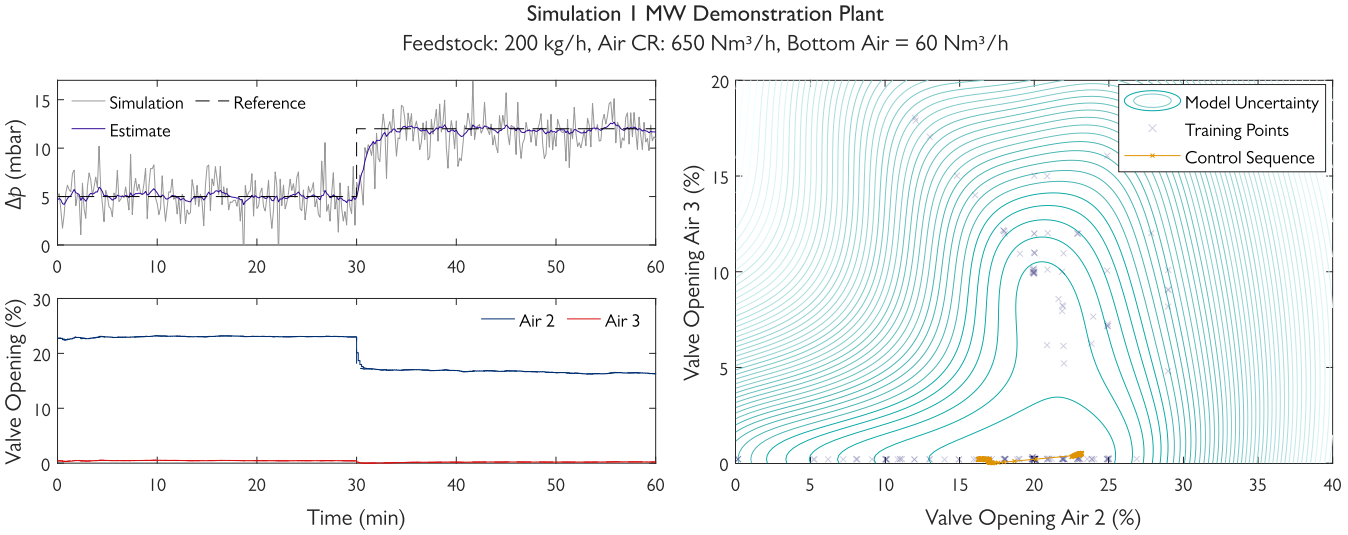

FIGURE 9. Closed-loop simulation for the 1 MW demonstration plant. The plots on the left show the controlled variable (top) and the control inputs (bottom). The plot on the right visualizes the GP uncertainty.

To gain insight into GP regression and to understand how individual inputs affect GP prediction, input variations are performed. The results are shown in Fig. 6 and Fig. 7 for the 100 kW pilot plant and the 1 MW demonstration plant, respectively. In these figures, the horizontal axes represent the varied inputs, while the vertical axes show the GP predictions. The line represents the mean, with dashed lines indicating regions where no training data is available. The shaded area around it represents the standard deviation of the prediction. The smaller plots below show the starting point from which the inputs are varied (shown in black) and the locations of the training data points (shown as colored bars).

According to the model, the circulation rate for both plants increases with higher feedstock feed rates. For the 100 kW plant, increasing the volume flow of air 1 results in increased circulation, which is expected as this air blows up the bed material. Conversely, increasing the volume flow of air 2 and air 3 decreases the circulation, probably because these air inlets are mounted facing downwards, opposing the circulation.

For the 1 MW plant, circulation increases with higher total airflow or, to a limited extend, increased bottom air volume flow. Opening the valves for air 2 or air 3 decreases circulation, as these actions increase the air fed to the reactor at higher positions, thus reducing the volume flow of air 1. Air 2 has a greater effect than air 3, possibly because the pipe diameter for air 3 is smaller, resulting in less air being diverted from air 1 when the air 3 valve is opened compared to when the air 2 valve is opened.

The dynamic components of the models incorporate time constants of $\tau_{100\text{kW}} = 10\,\text{s}$ and $\tau_{1\text{MW}} = 50\,\text{s}$, respectively.

B. CLOSED-LOOP SIMULATIONS

The control algorithm is validated in closed-loop simulations for both the 100 kW pilot plant and the 1 MW demonstration plant. The ANNs are used as simulation models.

1) 100 KW PILOT PLANT

For the 100 kW pilot plant, the controller parameters are chosen to be

$$\lambda = 10^{-2},\ \boldsymbol{R}_c = 5\boldsymbol{I},\ \sigma_{\text{GP,max}} = 0.5,$$

and the EKF parameters

$$\sigma_w^2 = 10^{-5},\ \sigma_v^2 = 0.85.$$

The controller was executed with a sampling time of $T_s = 2\,\text{s}$. The results of the closed-loop simulation for the 100 kW pilot plant are presented in Fig. 8. The upper plot depicts the solids circulation rate, indicated by the pressure difference in the upper CR. The gray line represents the simulated output, with noise introduced by adding a normally distributed random number with zero mean and variance σ_v^2. Reference changes occur at 5 min and 20 min. The second reference change is set to an unattainable level to demonstrate how infeasibility is handled using (23). The middle subplot shows the total airflow to the CR with its reference and the fuel input. The lower plot illustrates the three air volume flows, which are the control inputs. The dashed lines represent the steady-state inputs $\bar{\boldsymbol{u}}$, while the solid lines represent the control inputs $\boldsymbol{u}$ applied to the process.

2) 1 MW DEMONSTRATION PLANT

For the 1 MW demonstration plant, the controller parameters are chosen to be

$$\lambda = 10^{-2},\ \boldsymbol{R}_c = \boldsymbol{I},\ \sigma_{\text{GP,max}} = 3,$$

and the EKF parameters

$$\sigma_w^2 = 10^{-3},\ \sigma_v^2 = 3.3.$$

The controller operates with a sampling time of $T_s = 10\,\text{s}$.

Fig. 9 and 10 show the corresponding closed-loop simulation results. For this plant, which has two control inputs, the

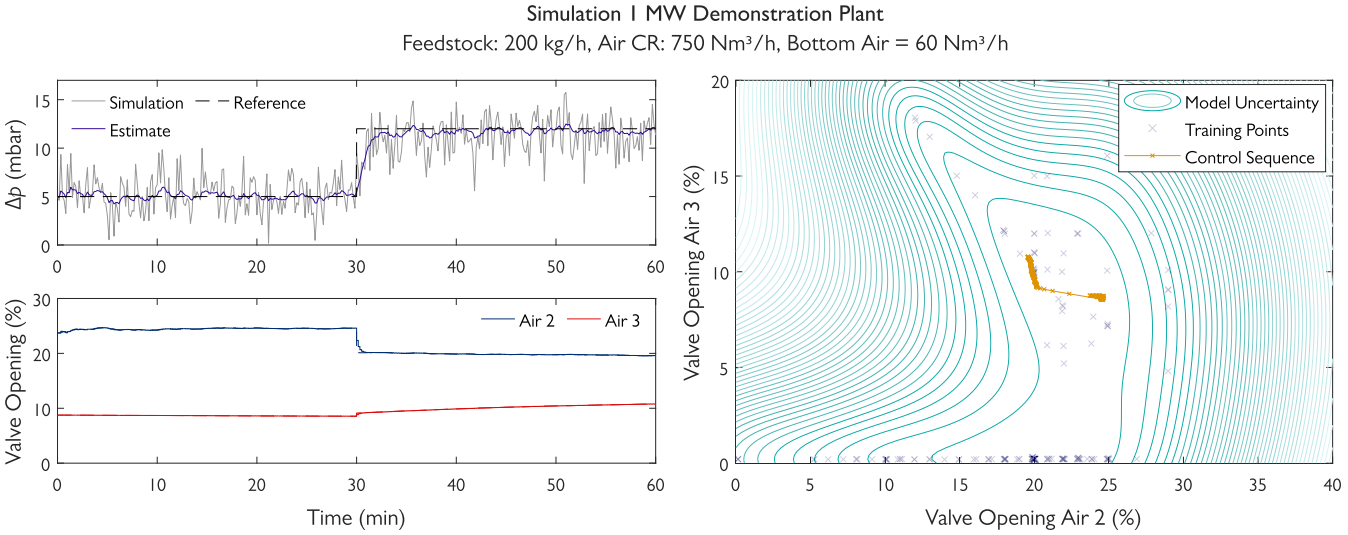

FIGURE 10. Closed-loop simulation for the 1 MW demonstration plant. Second simulation scenario with a different airflow to the CR.

model uncertainty can be visualized over the control input space, as shown in the contour plots in the right subplots. The training data points are also shown in these plots. This model uncertainty is affected by other model inputs - feed rate, airflow to the CR, and bottom airflow - which are not control inputs. Therefore, two separate simulations were conducted holding these three variables constant so that the model uncertainties over the control input space remain unchanged within each simulation. In the first simulation scenario, the lowest model uncertainty occurs when the air 3 valve is nearly closed and the air 2 valve is used to track changes in the reference. In contrast, in the second scenario, the model uncertainty is minimized when both valves are used for control.

The calculation times required for the closed-loop simulations are given in Table 2.

C. EXPERIMENTAL VALIDATION

The results of the experimental closed-loop validation for the 100 kW pilot plant are shown in Fig. 11. The controller parameters are identical to those used in the 100 kW pilot plant simulation. The controller was implemented in MATLAB, running on a separate computer, and receives measurement data from the process control system every 2 seconds. For clarity, a smoothed version of the solids circulation rate, represented by the pressure difference in the CR, is also shown in the plot. This was smoothed using a centered moving average with a window length of 20 samples. During the test run, the references for the solids circulation rate, the total airflow to the CR, and the feedstock feed rate were varied multiple times. Around 40 min into the run, the reference for the solids circulation rate was set to an unattainable level. In this case, the controller applied the maximum possible circulation rate while maintaining a maximum model uncertainty as specified by (23b).

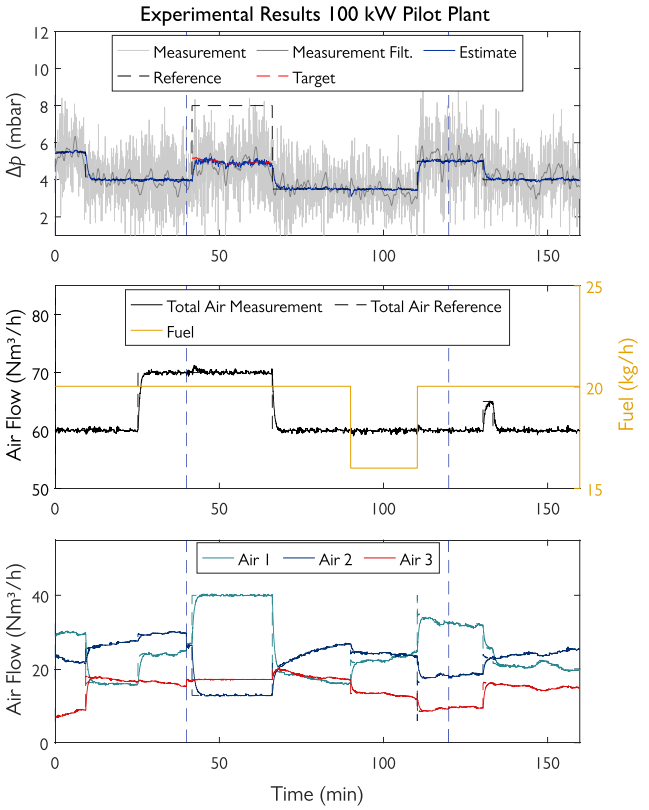

FIGURE 11. Experimental results of the GP regression-based controller applied to the DFB process at the 100 kW pilot plant at TU Wien.

The experiment was interrupted twice, as indicated by the vertical dashed lines.

The controller performed very well, effectively managing the variations and maintaining stable operation throughout the test run. This demonstrates the robustness and reliability of the control strategy under different operating conditions.

VI. CONCLUSION AND OUTLOOK

This study presents a method for modeling and controlling the solids circulation rate in DFB gasification using GP regression. By exploiting the uncertainty in the GP predictions, the process was driven toward regions of low model uncertainty, thereby improving the reliability and accuracy of control actions. Simulation results for both a 100 kW pilot plant and a 1 MW demonstration plant demonstrated the applicability of the method to different plants without extensive modeling efforts. The controller was successfully implemented in the 100 kW pilot plant and achieved offset-free tracking of constant references. This was achieved by incorporating a disturbance state into the model to compensate for plant model mismatch and unmeasured disturbances.

The controller presented can also be used as a subordinate controller, whereby the desired circulation is not specified directly by the plant operator, but by a higher-level controller that regulates temperatures or gas compositions.

In addition, the GP regression method employed in this study has potential for other applications. First, it could be used to identify regions of low data availability and high model uncertainty, facilitating the design of targeted identification experiments to improve model accuracy. Second, the control approach demonstrated here could be extended to similar processes, such as chemical looping combustion, where precise control of the solids circulation rate is critical.

REFERENCES

[1] H. Lee and J. Romero, Eds., *2023: Climate Change 2023: Synthesis Report. Contribution of Working Groups I, II and III to the Sixth Assessment Report of the Intergovernmental Panel on Climate Change*. Geneva, Switzerland: IPCC, pp. 35–115, doi: 10.59327/IPCC/AR6-9789291691647. [Online]. Available: https://www.ipcc.ch/report/ar6/syr/

[2] J. Karl and T. Pröll, "Steam gasification of biomass in dual fluidized bed gasifiers: A review," *Renew. Sustain. Energy Rev.*, vol. 98, pp. 64–78, Dec. 2018.

[3] A. Bartik, F. Benedikt, J. Fuchs, H. Hofbauer, and S. Müller, "Experimental investigation of hydrogen-intensified synthetic natural gas production via biomass gasification: A technical comparison of different production pathways," *Biomass Convers. Biorefinery*, vol. 14, no. 18, pp. 23091–23110, Sep. 2024.

[4] M. Hammerschmid, A. Bartik, F. Benedikt, M. Veress, S. Pratschner, S. Müller, and H. Hofbauer, "Economic and ecological impacts on the integration of biomass-based SNG and FT diesel in the Austrian energy system," *Energies*, vol. 16, no. 16, p. 6097, Aug. 2023.

[5] A. Chiodini, L. Bua, L. Carnelli, R. Zwart, B. Vreugdenhil, and M. Vocciante, "Enhancements in biomass-to-liquid processes: Gasification aiming at high hydrogen/carbon monoxide ratios for direct fischer-tropsch synthesis applications," *Biomass Bioenergy*, vol. 106, pp. 104–114, Nov. 2017.

[6] S. Müller, P. Groß, R. Rauch, R. Zweiler, C. Aichernig, M. Fuchs, and H. Hofbauer, "Production of diesel from biomass and wind power—Energy storage by the use of the fischer-tropsch process," *Biomass Convers. Biorefinery*, vol. 8, no. 2, pp. 275–282, Jun. 2018.

[7] M. Kraussler, M. Binder, P. Schindler, and H. Hofbauer, "Hydrogen production within a polygeneration concept based on dual fluidized bed biomass steam gasification," *Biomass Bioenergy*, vol. 111, pp. 320–329, Apr. 2018.

[8] J. Loipersböck, M. Luisser, S. Müller, H. Hofbauer, and R. Rauch, "Experimental demonstration and validation of hydrogen production based on gasification of lignocellulosic feedstock," *ChemEngineering*, vol. 2, no. 4, p. 61, Dec. 2018.

[9] K. Göransson, U. Söderlind, and W. Zhang, "Experimental test on a novel dual fluidised bed biomass gasifier for synthetic fuel production," *Fuel*, vol. 90, no. 4, pp. 1340–1349, Apr. 2011.

[10] J. Fuchs, J. Schmid, F. Benedikt, A. Mauerhofer, S. M´uller, and H. Hofbauer, "A general method for the determination of the entrainment in fluidized beds," *Int. J. Multiphys.*, vol. 12, pp. 359–372, Nov. 2018.

[11] H. Liu, R. J. Cattolica, and R. Seiser, "Operating parameter effects on the solids circulation rate in the CFD simulation of a dual fluidized-bed gasification system," *Chem. Eng. Sci.*, vol. 169, pp. 235–245, Sep. 2017.

[12] J. Gu, Y. Shao, X. Liu, W. Zhong, and A. Yu, "Modelling of particle flow in a dual circulation fluidized bed by a Eulerian-Lagrangian approach," *Chem. Eng. Sci.*, vol. 192, pp. 619–633, Dec. 2018.

[13] L. Stanger, A. Schirrer, F. Benedikt, A. Bartik, S. Jankovic, S. Müller, and M. Kozek, "Dynamic modeling of dual fluidized bed steam gasification for control design," *Energy*, vol. 265, Feb. 2023, Art. no. 126378.

[14] C. Williams and C. Rasmussen, "Gaussian processes for regression," in *Advances in Neural Information Processing Systems*, vol. 8. Cambridge, MA, USA: MIT Press, 1995.

[15] R. Murray-Smith and D. Sbarbaro, "Nonlinear adaptive control using nonparametric Gaussian process prior models," *IFAC Proc. Volumes*, vol. 35, pp. 325–330, Dec. 2002.

[16] G. Gregorcic and G. Lightbody, "Internal model control based on a Gaussian process prior model," in *Proc. Amer. Control Conf.*, vol. 6, 2003, pp. 4981–4986.

[17] J. Kocijan, R. Murray-Smith, C. E. Rasmussen, and A. Girard, "Gaussian process model based predictive control," in *Proc. Amer. Control Conf.*, 2004, pp. 2214–2219.

[18] L. Stanger, A. Schirrer, A. Bartik, and M. Kozek, "Minimum-variance model predictive control for dual fluidized bed circulation control," *IFAC-PapersOnLine*, vol. 56, no. 2, pp. 2701–2706, 2023.

[19] L. Stanger, A. Bartik, M. Hammerschmid, S. Jankovic, F. Benedikt, S. Müller, A. Schirrer, S. Jakubek, and M. Kozek, "Model predictive control of a dual fluidized bed gasification plant," *Appl. Energy*, vol. 361, May 2024, Art. no. 122917.

[20] N. Hanchate, S. Ramani, C. S. Mathpati, and V. H. Dalvi, "Biomass gasification using dual fluidized bed gasification systems: A review," *J. Cleaner Prod.*, vol. 280, Jan. 2021, Art. no. 123148.

[21] J. C. Schmid, "Development a novel dual fluidized bed gasification system for increased fuel flexibility," Ph.D. dissertation, Inst. Chem., Environ. Biosci. Eng., TU Wien, Vienna, Austria, 2014.

[22] F. Benedikt, "Fuel flexible advance dual fluidized bed steam gasification," Ph.D. dissertation, Inst. Chem., Environ. Biosci. Eng., TU Wien, Vienna, Austria, 2020.

[23] D. Kadlez, F. Benedikt, M. Huber, K. Fürsatz, J. Schmid, H. Hofbauer, and S. Müller, *Technology Development of Advanced Dual Fluidized Bed Steam Gasification From Pilot To Demonstration Scale First Results From a 1 Mw Demonstration Plant*, document SSRN 4763693, 2024.

[24] D. Hochstöger, "Performance evaluation of DFB gas generation based on a comparison of two research plants with 100 kW and 1 MW," M.S. thesis, Inst. Chem., Environ. Biosci. Eng., TU Wien, Vienna, Austria, 2023.

[25] J. Schmid, C. Pfeifer, H. Kitzler, T. Pröll, and H. Hofbauer, "A new dual fluidized bed gasifier design for improved in situ conversion of hydrocarbons," in *Proc. Int. Conf. Polygeneration Strateg.*, 2011, pp. 1–18.

[26] X. Liu, M. Zhang, S. Zhang, Y. Ding, Z. Huang, T. Zhou, H. Yang, and G. Yue, "Measuring technologies for CFB solid circulation rate: A review and future perspectives," *Energies*, vol. 15, no. 2, p. 417, Jan. 2022.

[27] A. Kreuzeder, C. Pfeifer, and H. Hofbauer, "Fluid-dynamic investigations in a scaled cold model for a dual fluidized bed biomass steam gasification process: Solid flux measurements and optimization of the cyclone," *Int. J. Chem. React. Eng.*, vol. 5, no. 1, pp. 1–8, Aug. 2007.

[28] T. Karlsson, X. Liu, D. Pallarès, and F. Johnsson, "Solids circulation in circulating fluidized beds with low riser aspect ratio and varying total solids inventory," *Powder Technol.*, vol. 316, pp. 670–676, Jul. 2017.

[29] S. Matsuda, "Measurement of solid circulation rate in a circulating fluidized bed," *Powder Technol.*, vol. 187, no. 2, pp. 200–204, Oct. 2008.

[30] X. Liu, Y. Zhang, H. Yang, X. Liu, Y. Zhang, and G. Yue, "A method for measuring the solid circulation rates of CFB boilers based on the particle flow-around principle," *Chem. Eng. J.*, vol. 481, Feb. 2024, Art. no. 148424.

[31] Y. Alghamdi, Z. Peng, K. Shah, B. Moghtaderi, and E. Doroodchi, "Predicting the solid circulation rate in chemical looping combustion systems using pressure drop measurements," *Powder Technol.*, vol. 286, pp. 572–581, Dec. 2015.

[32] M. Stollhof, S. Penthor, K. Mayer, and H. Hofbauer, "Estimation of the solid circulation rate in circulating fluidized bed systems," *Powder Technol.*, vol. 336, pp. 1–11, Aug. 2018.

[33] C. E. Rasmussen and C. K. I. Williams, *Gaussian Processes for Machine Learning*. Cambridge, MA, USA: MIT Press, 2006.
[34] M. N. Gibbs, "Bayesian Gaussian processes for regression classification," Ph.D. dissertation, Univ. Cambridge, Cambridge, England, 1997.
[35] C. E. Rasmussen and C. K. I. Williams, *Gaussian Processes for Machine Learning*. Cambridge, MA, USA: MIT Press, 2005.
[36] Mathworks Inc. (2023). *MATLAB Deep Learning Toolbox*. [Online]. Available: https://www.mathworks.com/products/deep-learning.html
[37] M. Grewal and A. Andrews, *Kalman Filtering: Theory and Practice Using MATLAB*. Hoboken, NJ, USA: Wiley, 2008.
[38] M. D. Mckay, R. J. Beckman, and W. J. Conover, "A comparison of three methods for selecting values of input variables in the analysis of output from a computer code," *Technometrics*, vol. 42, no. 1, p. 55, Feb. 2000.
[39] Mathworks Inc. (2023). *MATLAB Optimization Toolbox*. [Online]. Available: https://www.mathworks.com/products/optimization.html
[40] MathWorks Inc. (2023). *MATLAB Statistics and Machine Learning Toolbox*. [Online]. Available: https://www.mathworks.com/products/statistics.html

LUKAS STANGER received the master's degree in mechanical engineering-management from TU Wien, Vienna, Austria, in 2021, where he is currently pursuing the Ph.D. degree. Since 2021, he has been a member of the Project Team with the Institute of Mechanics and Mechatronics, TU Wien. His research interests include modeling, control, and optimization, with a recent focus on energy systems.

ALEXANDER BARTIK received the Ph.D. degree in chemical engineering from TU Wien, in 2024. He is currently a Postdoctoral Researcher with the Institute of Chemical, Environmental, and Bioscience Engineering. His research interests include biomass gasification technologies and downstream synthesis processes employing experimental and simulation-based methods.

MATTHIAS BINDER received the M.Sc. degree in process and chemical engineering from TU Wien. Since 2015, he has been with the BEST-Bioenergy and Sustainable Technologies in the field of syngas platform technologies, including gasification, gas cleaning, and downstream synthesis applications. His dissertation is dedicated to mixed alcohol synthesis based on biomass steam gasification with TU Wien.

ALEXANDER SCHIRRER received the M.S., Ph.D., and Habilitation degrees in mechanical engineering from TU Wien, Vienna, Austria, in 2007, 2011, and 2018, respectively. Since 2023, he has been a Senior Scientist with the Institute of Mechanics and Mechatronics, TU Wien. His research interests include modeling, simulation, optimization, and control of complex and distributed-parameter systems.

STEFAN JAKUBEK received the M.Sc. degree in mechanical engineering, the Ph.D. degree in technical sciences, and the Habilitation (professorial qualification) degree in control theory and system dynamics from TU Wien, Vienna, Austria, in 1997, 2000, and 2007, respectively. From 2006 to 2009, he was the Head of Development of the Hybrid Powertrain Calibration and Battery Testing Technology, Automotive Industry Company AVL List GmbH, Graz, Austria. He is currently a Professor and the Head of the Institute of Mechanics and Mechatronics, TU Wien. His research interests include fault diagnosis, nonlinear system identification, and simulation technology.

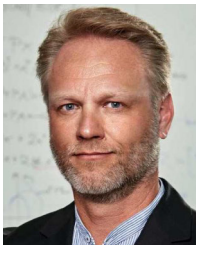

MARTIN KOZEK received the M.S. degree in mechanical engineering, and the Ph.D. and Habilitation degrees from TU Wien, Vienna, Austria, in 1994, 2000, and 2009, respectively. He is currently a Professor with the Institute of Mechanics and Mechatronics, TU Wien. His research interests include nonlinear systems modeling and identification, model predictive process control, and active control of structural vibrations.